

Towards Rapid Prototyping and Comparability in Active Learning for Deep Object Detection

Tobias Riedlinger^{*1} Marius Schubert^{*1} Karsten Kahl¹ Hanno Gottschalk¹ Matthias Rottmann^{1,2}

¹ School of Mathematics and Natural Sciences, IZMD, University of Wuppertal, Germany

² School of Computer and Communication Sciences, CVLab, EPFL, Switzerland

{riedlinger@math., mschubert@, kkahl@math., hgottsch@, rottmann@math.}uni-wuppertal.de

Abstract

Active learning as a paradigm in deep learning is especially important in applications involving intricate perception tasks such as object detection where labels are difficult and expensive to acquire. Development of active learning methods in such fields is highly computationally expensive and time consuming which obstructs the progression of research and leads to a lack of comparability between methods. In this work, we propose and investigate a sandbox setup for rapid development and transparent evaluation of active learning in deep object detection. Our experiments with commonly used configurations of datasets and detection architectures found in the literature show that results obtained in our sandbox environment are representative of results on standard configurations. The total compute time to obtain results and assess the learning behavior can thereby be reduced by factors of up to 14 when comparing with Pascal VOC and up to 32 when comparing with BDD100k. This allows for testing and evaluating data acquisition and labeling strategies in under half a day and contributes to the transparency and development speed in the field of active learning for object detection.

1. Introduction

Deep learning requires large amounts of data, typically annotated by vast amounts of human labor [4, 17, 40]. In particular in complex computer vision tasks such as object detection (OD), the amount of labor per image can lead to substantial costs for data labeling. Therefore, it is desirable to avoid unnecessary labeling effort and to have a rather large variability of the database. *Active learning* (AL) [30] is one of the key methodologies that aims at labeling the data that matters for learning. AL alternates model training and data labeling as illustrated in Fig. 1. At the core of each AL method is a query strategy that decides after

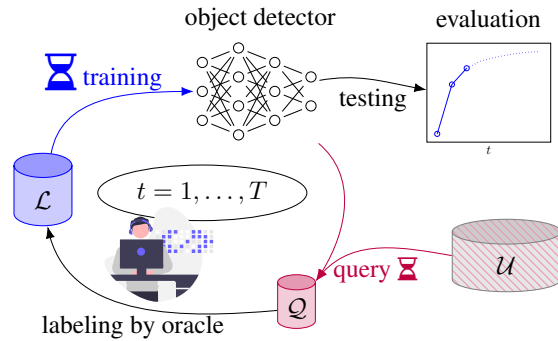


Figure 1: The generic pool-based AL cycle consisting of training on labeled data \mathcal{L} , querying informative data points \mathcal{Q} out of a pool of unlabeled data \mathcal{U} and annotation by a (human) oracle. In practice, training compute time is orders of magnitude larger than evaluating the AL strategy itself.

each model training which unlabeled data to query for labeling. The computation cost of AL is in general at least an order of magnitude higher than ordinary model training and so is its development [17, 33], which comprises several AL experiments involving T query steps with different parameters, ablation studies, etc. Hence, it is notoriously challenging to develop new AL methods for applications where model training itself is already computationally costly. In the field of OD, a number of works overcame this cumbersome hurdle [3, 6, 9, 10, 14, 22, 25, 28, 32, 35, 39]. However, these works did so in very different settings which makes their comparison difficult. Hence, it is difficult to give any advice for practitioners, which AL method to choose. Besides that, AL with real-world data may suffer from other influencing factors, *e.g.*, the quality of labels to which end fundamental research is conducted on AL in presence of label errors [1, 2, 36, 37]. These observations demand for a development environment that enables rapid prototyping, cutting down to the huge computational efforts of AL in object detection and fostering comparability of different AL

^{*}Equal contribution

methods.

Contribution. In this work, we propose a development environment that drastically cuts down the computational cost of developing AL methods. We do so by reducing the complexity of the deep object detectors as well as the complexity of the data base, establishing a non-trivial sandbox for deep OD. To this end, we construct a) two datasets that generalize MNIST digits [15] and EMNIST letters [7] to the setting of OD by pasting colored and transformed samples into background images from MS-COCO [19] and b) a selection of suitable small-scale object detectors. We justify this step and underline its value for the field of AL in OD. To do so, we conduct several experiments which show that results on our datasets generalize to a similar degree to established but more complex datasets (Pascal VOC [11] and BDD100k [38]), as they generalize among each other. We also demonstrate that we reduce the computational effort of AL experiments by factors of up to 32. In addition, to establish further comparability of AL methods for OD, we propose an extensive evaluation protocol. We summarize our contributions as follows:

- We propose a sandbox environment with two datasets, multiple networks, active learning queries and an extensive evaluation protocol. This setup allows for broader comparisons and detailed and transparent experiment tracking at lowered computational effort. We demonstrate this with extensive numerical results.
- We analyze the generalization capabilities of our sandbox and find that results obtained by our sandbox generalize well to Pascal VOC and BDD100k.
- We contribute to future AL development by providing an implementation of our pipeline in a flexible environment as well as an automated framework for evaluation and visualization of results.

Code will be publicly available at `GitHub`. All selected configurations and hyperparameters in addition to evaluation files for the experiments conducted will be published in order to facilitate future comparisons with the implemented baselines.

The remainder of this work is structured as follows: Section 2 contains a summary of the literature in fully-supervised AL for OD and how the present work relates to it. In Section 3 we introduce our sandbox setup for AL in OD, methods involved in our experiments and our proposed evaluation metrics. Section 4 first introduces our experimental setup. We investigate the degree to which AL in OD is comparable in Section 4.1 by studying different cases. Afterwards, in Section 4.2 we investigate rank correlations between AL on different datasets to measure the degree of similarity between the results. In Section 4.3, we

show time measurements to estimate the speed-up provided by our sandbox environment. Finally, we close with a summary of conclusions we draw from the empirical evidence in Section 5.

2. Related Work

Numerous methods of AL have been, and still are, developed in the classification setting and largely fall into two main categories. Uncertainty-based query strategies rely on the informativeness of a probabilistic model’s current prediction uncertainty [16]. In probabilistic classification models, popular examples include the probability margin [27], ensemble entropy [8], or committee disagreement [31]. A different approach is taken by density-based query strategies, which aim at exploiting data diversity between already known data and prospective queries. Typically, such methods are related to clustering algorithms [21, 29, 34] which can also be used in conjunction with uncertainty estimation methods. For a general overview of different AL approaches see e.g. [30].

The task of OD is more complex than image classification in that the background needs to be distinguished against foreground instances and each foreground instance needs to be assigned its own localization and classification. Not only does this require the choice of additional hyperparameters for making predictions, but this also entails more complex and expensive labels. Therefore, AL plays also a large role in OD. Yoo and Kweon [35] present a task-agnostic method where a loss prediction module estimates a loss for every potentially queried image and selects the images for which the largest loss is expected. Brust *et al.* [3] estimate prediction-wise uncertainty by the probability margin and aggregate to image uncertainty by the summation, averaging or taking the maximum. For a black-box approach, Roy *et al.* [25] follow the same idea, but with using the classification entropy as prediction uncertainty. Moreover, they propose a white-box approach which is inspired by query-by-committee, making use of predictions at different scales in the object detector. In general, an ensemble of OD heads, trained independently on the same set of labeled images, can be used to estimate prediction-wise classification uncertainty, *i.e.* mutual information based on entropies [14], or a combination of localization and classification uncertainty due to region of interest similarities [28]. But in particular, as training a variety of detector heads in each AL step is very costly, committee/ensemble query methods tend to be approximated by Monte Carlo (MC) Dropout [12, 13]. Some methods yield to custom object detectors, *i.e.* a Gaussian mixture model based object detector with an adjusted loss [6] or they intervene at least in the training pipeline, *e.g.* by suppressing noisy instances [39]. Another class of approaches is based on semi-supervised learning, *i.e.* incorporating either pseudo-labels for some representative

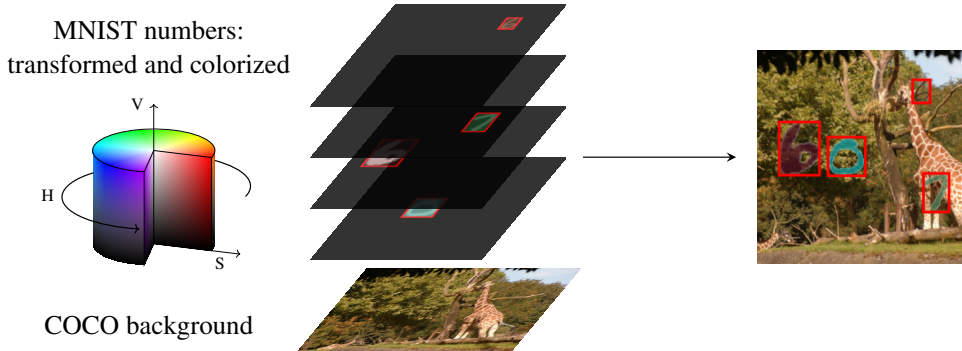


Figure 2: Generation scheme of semi-synthetic object detection data from MNIST digits on a non-trivial background image from MS-COCO.

easy samples to prevent distribution drift [10]. Alternatively used “weak” labels consist only of the center coordinates [9, 22, 32]. In this paper we compare uncertainty-based methods with each other that are exclusively based on fully supervised training [3, 6, 14, 25]. These works are difficult to compare since the datasets, network architectures, frameworks, initial dataset sizes, query sizes and hyperparameters for training and inference heavily differ from each other. Unlike the works mentioned, we aim at putting the AL task itself on equal footing between different settings to improve development speed and evaluation transparency. In our work, we compare some of the above-mentioned methods to each other based on the same configurations for frequently used datasets and network architectures. Comparative investigations of this kind has escaped previous research in the field.

3. A Sandbox Environment with Datasets, Models and Evaluation Metrics

In this section we describe the objective of AL and also our sandbox environment. The main setting we propose consists of two semi-synthetic OD datasets and down-scaled versions of standard object detectors leaving the detection mechanism unchanged. Additionally, we introduce evaluations capturing different aspects of the observed AL curve.

3.1. Active Learning

The term active learning refers to a setup (*cf.* Fig. 1) where only a limited amount of fully annotated data \mathcal{L} is available together with a task-specific model. In addition, there is a pool or a stream of unlabeled data \mathcal{U} from which the model queries those samples \mathcal{Q} which are most informative. Success of the query strategy is measured by observing that training on the new data pool leads to an increase of test performance higher than another method. Afterwards, \mathcal{Q} is annotated by an oracle (usually a human worker), added to \mathcal{L} and the model is fine-tuned or fitted from scratch on

\mathcal{L} from where the cycle continues. Before each acquisition step, the current model performance is evaluated which leads to graphs like the ones in Fig. 3. The query step can take diverse algorithmic forms, see Section 2 or [30].

3.2. Datasets

We construct an OD problem by building a synthetic overlay to images from the real-world MS-COCO dataset (*cf.* Fig. 2), which constitutes the data of our sandbox. COCO images with deleted annotations provide a realistic, feature-rich background on which foreground objects shall be recognized. As foreground, we utilize two sets of categories: MNIST digits and EMNIST letters. We apply randomized coloration and opacity to foreground instances such that trivial edge detection becomes unfeasible. Colors are drawn from HSV space uniformly by $(h, s, v) \sim U([0.0, 1.0] \times [0.05, 1.0] \times [0.1, 1.0])$ which yielded the best optical variability. The chosen HSV-color is multiplied with the gray scale value of the original image avoiding the instances being monochromatic. Opacity is similarly drawn uniformly $\alpha \sim U([0.5, 0.9])$ and in addition, we apply image translation, scaling and shearing to all numbers/letters. The number of instances per background image is Poisson-distributed with mean $\lambda = 3$. Tight bounding box (and instance segmentation) annotations can be obtained from the original transformed gray scale (E)MNIST images and the category label can be adopted. Compared to simple detection datasets such as SVHN [20], the geometric variety in our datasets is more similar to those of OD benchmarks such as Pascal VOC or MS-COCO. The reduction in the dataset complexity allows for the achievement of decent performance even for small architectures and leads to quickly converging training and low inference times. In the following we use the terms “MNIST-Det” and “EMNIST-Det” to refer to our OD datasets.

Table 1: Exemplary object detection architectures with backbone configurations employed in the experiments and associated number of parameters.

Detector	Backbone	# params	Backbone	# params
RetinaNet	ResNet50	36.5M	ResNet18	20.1M
Faster R-CNN	ResNet101	60.2M	ResNet18	28.3M
YOLOv3	Darknet53	61.6M	Darknet20	10.3M

3.3. Models

Modern OD architectures utilize several conceptually different mechanisms to solve the detection task. Irrespective of the amount of accessible data, some applications of OD may require high inference speed while others may require a large degree of precision or some trade-off between the two. The type of architecture as well, as the underlying detection mechanism are, however, disjoint to some degree from the depth of the feature extraction in the backbone. The latter is mainly responsible for the quality and resolution of features. We use this insight to down-scale architectures for AL by reducing the network depth while keeping the detection mechanism in the network’s head unchanged. Together with the simplified OD objectives from Section 3.2, we obtain a well-performing, low-capacity and fast-inference setup to study AL with the same OD mechanisms that occur in practice. Tab. 1 shows the choices for a YOLOv3 [23], RetinaNet [18] and Faster R-CNN [24] setup, which we have made for our investigations together with the resulting number of parameters. The number of parameters in the standard setup was reduced by up to a factor of around 6 leading to a significant decrease in training and inference time.

3.4. Active Learning Methods in Object Detection

For the construction of baseline AL methods, we focus on querying whole images instead of single bounding boxes. The latter would introduce an additional dimension of complexity where unlabeled image regions need to be ignored. The frequently used uncertainty-based query strategies from image classification, such as entropy, probability margin, MC dropout, and mutual information, determine prediction-specific but not image-wise uncertainties. Hence, we introduce an aggregation step to obtain image-wise query scores.

For a given image \mathbf{x} , a neural network predicts a fixed number N of bounding boxes $\hat{b}_{\mathbf{x}}^{(i)} = \{x_{\min}, y_{\min}, x_{\max}, y_{\max}, s, p_1, \dots, p_C\}$, $i = 1, \dots, N$, where $x_{\min}, y_{\min}, x_{\max}, y_{\max}$ represent the localization, s the objectness score (or analog) and p_1, \dots, p_C the class probabilities for the C classes of the prediction. Only the set of boxes that remain after non maximum suppression (NMS) and score thresholding are used to determine pre-

diction uncertainties. Already the choice of the parameters for the NMS and the score threshold influence the queries, since they decide which (uncertain) predictions remain.

Given a prediction \hat{b} we compute its classification entropy $H(\hat{b}) = -\sum_{c=1}^C p_c \cdot \log(p_c)$ and its probability margin score $PM(\hat{b}) = (1 - [p_{c_{\max}} - \max_{c \neq c_{\max}} p_c])^2$. Here, c_{\max} denotes the class with the highest predicted probability. When dropout is implemented in the architecture, Monte-Carlo Dropout samples can be drawn at inference time where the output of the same anchor box $\hat{b}_1, \dots, \hat{b}_K$ are sampled K times. The final prediction under dropout is then the arithmetic mean $\bar{\hat{b}} = \frac{1}{K} \sum_{i=1}^K \hat{b}_i$. The Monte-Carlo mutual information is estimated by $MI(\hat{b}) = H(\bar{\hat{b}}) - \overline{H(\hat{b})}$ with the second term being the average entropy of the individual samples. We also regard the maximum feature standard deviations within \hat{b} by first standardizing variances over all query predictions to treat localization and classification features on the same footing. The dropout uncertainty is then $D = \max_{\phi \in \{x_{\min}, y_{\min}, x_{\max}, y_{\max}, s, p_1, \dots, p_C\}} \sigma(\hat{\phi})$. Note that for all these methods, uncertainty is only considered in the predicted foreground instances. Since the uncertainty-based selection strategies only determine prediction-based uncertainties, either the sum, average, or maximum is taken over predicted instances to obtain a final query score for the image. Summation, for instance, tends to prefer images with a large amount of instances while averaging is strongly biased by the thresholds (imagine considering many false positive predictions which could be filtered by a higher threshold). In the presented experiments, we use summation and further aggregations are investigated in the appendix. Additionally, we also regard random acquisition as a completely uninformed query baseline.

Diversity-based methods make use of latent activation features in neural networks which heavily depend on the OD architecture. Since purely diversity-based methods have been less prominent in the literature, we focus on the more broadly established uncertainty baselines.

3.5. Evaluation

Model Performance. In the literature, methods are frequently evaluated by counting the number of data samples needed to cross some fixed reference performance mark. For OD, performance is usually measured in terms of the mAP_{50} metric for which there is a maximum value known when training on all available data. In AL then, some percentage of this maximal performance, e.g., 90% needs to be reached with as few data points as possible. Collecting performance over amount of queried data gives rise to curves such as the one in the top right of Fig. 1 which we call *AL curves* in the following.

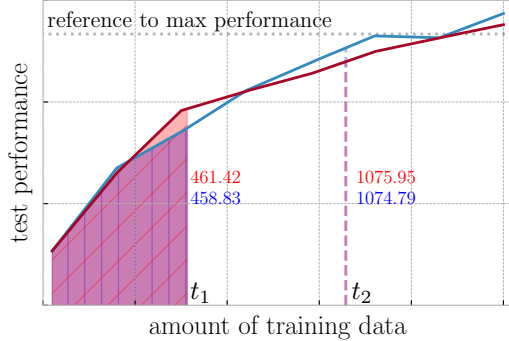


Figure 3: Area under AL curve (AUC) metric at different stages of an AL curve for two different query strategies (averaged, taken from Fig. 4).

Counting Annotations. “Amount of training data” usually translates to the number of queried images which is set as a hyperparameter and fixed for each method and AL cycle. Considering that in the annotation process, each bounding box needs to be labeled and there tends to be high variance in the number of instances per image in common benchmark datasets, it is not clear whether to measure annotated data in terms of images or instances. Therefore, we stress that the scaling of the t -axis is important especially in instance-wise prediction tasks such as OD. Both views, counting images or instances, can be argued for. Therefore, we evaluate the performance of each result not only based on the acquired images, but also transform the t -axis under the curves to the number of annotated instances. By linear interpolation between query points and averaging of individual seeds of the same experiment, we obtain image- or instance-wise standard deviations of the performance.

Area under AL Curves. In light of the complexity of the AL problem, we propose the area under the AL curve (AUC). It constitutes a more robust performance metric compared to (horizontal or vertical) cross sections through the learning curves. Fig. 3 shows two AL curves and corresponding AUC metrics at two distinct points t_1 and t_2 . Note that in practice, there is no fixed maximal dataset size for which a maximum performance exists. Then, the AL experiment may end and be evaluated at any given vertical section of t points of training data. Knowing the maximal performance (or the 90% mark shown in Fig. 3) may lead to wrong conclusions in the presented case which is taken from the scenario in Fig. 4. Ending the experiment at t_1 clearly determines the red curve (which also has a higher AUC) as preferable. Ending the experiment at t_2 favors the blue curve by just looking at the actual test performance. However, the AUC still favors the red curve, since it takes the complete AL curve into account. This is in line with our qualitative feeling of the curves when regarded up to t_2 .

Table 2: Maximum mAP_{50} values achieved by the models in Tab. 1 on the respective datasets (standard-size detectors on VOC and BDD; sandbox-size on (E)MNIST-Det). The entire available training data is used.

	YOLOv3	RetinaNet	Faster R-CNN
MNIST-Det	0.962	0.908	0.937
EMNIST-Det	0.959	0.919	0.928
Pascal VOC	0.794	0.748	0.797
BDD100k	0.426	0.464	0.525

Note that we use the AUC metric for calculating rank correlations in Section 4.2. The raw results of the AUC metric are shown in the appendix.

4. Experiments

In this section, we present results of experiments with our sandbox environment as well as established datasets, namely Pascal VOC and BDD100k, in the following abbreviated as VOC and BDD. We do so by presenting AL curves, summarizing benchmark results and discussing our observations for different evaluation metrics in Section 4.1. We then show in Section 4.2 quantitatively that our sandbox results generalize to the same extent to VOC and BDD as results obtained on those datasets generalize between each other. In other words, we demonstrate the dataset-wise representativity of the results obtained by our sandbox. Thereafter, this is complemented with a study on the computational speedup in Section 4.3 when using the sandbox instead of VOC or BDD.

Implementation. We implemented our pipeline in the open source MMDetection [5] toolbox. In our experiments for VOC, \mathcal{U} initially consists of “2007 train” + “2012 train-val” and we evaluate performance on the “2007 test”-split. At initialization, we randomly sample \mathcal{L} as a small portion of \mathcal{U} . When tracking validation performance to assure convergence, we evaluate on “2007 val”. Since BDD is a hard detection problem, we filtered frames with “clear” weather condition at “daytime” from the “train” split as initial pool \mathcal{U} yielding 12,454 images. We apply the same filter to the “val” split and divide it in half to get a test dataset (882 images for performance measurement) and a validation dataset (882 images for convergence tracking). For the (E)MNIST-Det datasets we generated 20,000 train images, 500 validation images and 2,000 test images. For reference, we collect in Tab. 2 the achieved performance of the respective models for each dataset which determines the 90% mark investigated in our experiments. Details on the architectures and concrete parameters for the AL experiments conducted are provided in the appendix.

Table 3: Amount of queried images and bounding boxes necessary to cross the 90% performance mark during AL. Lower values are better. Bold numbers indicate the lowest amount of data per experiment and underlined numbers are the second lowest.

		# queried images				# queried bounding boxes			
		MNIST-Det	EMNIST-Det	Pascal VOC	BDD100k	MNIST-Det	EMNIST-Det	Pascal VOC	BDD100k
YOLOv3	Random	327.9	595.6	2236.8	5871.2	1079.1	1825.3	5344.2	116362.1
	Entropy	245.5	398.8	<u>1732.8</u>	5389.3	1004.9	1583.0	4695.4	110694.9
	Prob. Margin	256.2	429.0	1858.5	4895.2	<u>1013.7</u>	1617.1	<u>4787.6</u>	100376.3
	MC Dropout	256.3	416.2	1679.4	<u>5200.5</u>	1115.3	1671.6	4875.1	<u>110427.6</u>
	Mutual Inf.	<u>249.8</u>	<u>399.5</u>	1884.2	5912.9	1061.9	<u>1602.7</u>	5527.0	125050.1
Faster R-CNN	Random	450.0	843.4	1293.7	6434.3	2140.0	2891.7	3125.2	129219.0
	Entropy	384.5	561.6	1030.6	5916.7	1608.4	2156.4	2707.0	123008.6
	Prob. Margin	408.7	626.2	<u>1036.5</u>	5761.6	<u>1622.9</u>	2285.1	<u>2711.6</u>	117889.3
	MC Dropout	<u>390.5</u>	647.4	1127.5	6296.4	1818.1	2773.8	3624.7	130533.8
	Mutual Inf.	395.3	<u>572.6</u>	1080.2	6385.7	1695.6	<u>2235.3</u>	3026.5	132855.7

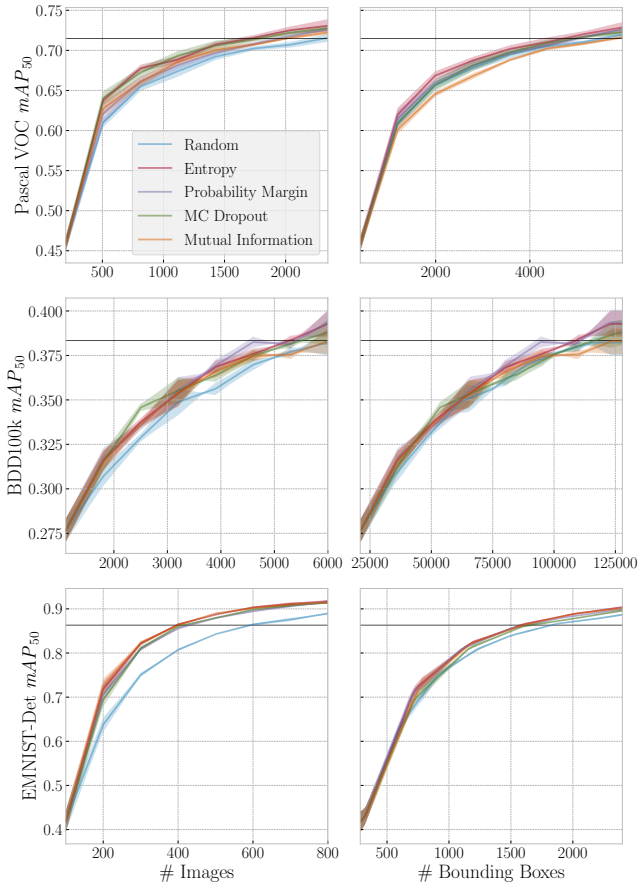


Figure 4: Comparison of YOLOv3 AL curves on three different datasets.

4.1. Benchmark Results

We first investigate differences in AL results w.r.t. the datasets where we fix the architecture. The comparison

uses the YOLOv3 detector on two standard OD benchmarks (VOC and BDD) and our EMNIST-Det dataset. Our comparison includes the five query baselines described in Section 3.4. We obtain AL curves averaged over four random initializations and evaluated in terms of queried images as well as in terms of queried object instances, respectively. Fig. 4 shows the test performance curves with shaded regions indicating point-wise standard deviations. The left panels show performance according to queried images while the right panels show the same curves but according to queried instances. We observe that the uncertainty-based query strategies tend to consistently outperform the Random query in image-wise evaluation. However, when regarding the number of queried bounding boxes, the situation is far less clear. For EMNIST-Det, the difference between the Random and the uncertainty-based queries decreases substantially, such that only a marginal difference is visible. In VOC and BDD, the Random baseline falls roughly somewhere in-between the uncertainty baselines in instance-wise evaluation. This indicates that greedy acquisition of images with highest sum of uncertainty tends to query images with a large amount of ground truth boxes. Obtaining many ground truth signals improves detection performance in these cases, while the query of large amounts of boxes gives rise to a higher annotation cost on the right panels. From this observation, we conclude that comparing AL curves based only on the number of acquired training images gives an incomplete impression of the method and the associated annotation costs. In addition to the image-wise evaluation, an instance-wise evaluation should be considered. Note also, that the AL curves for EMNIST-Det and VOC have a smoother progression than those for BDD. We attribute this finding to the fact that BDD is a far more complicated detection problem which includes a large amount of small objects. However, the fluctuations in the AL curves on BDD tend to average out as we consider the AUC of the

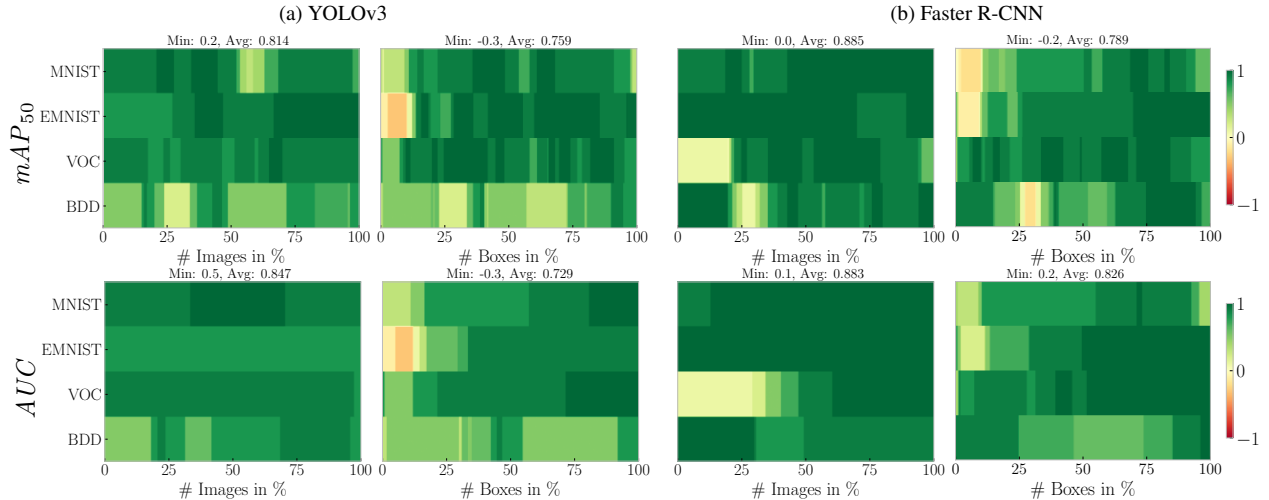


Figure 5: Curves of rank correlations between the cumulative AUC and the final rankings at the 90% max performance mark.

AL curve as evaluation metric. This becomes clear in light of the results in Section 4.2, where we study the generalization across datasets in terms of the AUC of the AL curve.

In Tab. 3 we show extended benchmark results. For each detector to reach 90% of the maximum performance, the table shows the number of queried images required, resp. the number of bounding boxes for each method. These numbers were acquired as the average of four runs. We see the rankings per experiment which often favor the Entropy baseline, however, the overall rankings are rather unstable throughout the table. Note in particular, that for the arguably hardest detection problem BDD, the Random baseline beats the Mutual Information baseline for the YOLOv3 detector. In the analog setting for Faster R-CNN the image-wise margin of the Mutual Information becomes slim. This observation also holds for instance-wise evaluation and is even more pronounced where in six cases, Random beats an informed query baseline. Results for the RetinaNet detector can be found in the appendix. In light of the discussion in Section 3.5, we conclude that in order to assess the viability of a query strategy, AL curves should be viewed from both angles: performance over number of images and over number of bounding boxes queried.

4.2. Generalization of Sandbox Results

Instead of evaluating the pure performance at each AL step we have proposed in Section 3.5 to compute the corresponding AUC as a more robust metric of AL performance. With respect to the final method ranking at some fixed reference mark, we compute Spearman rank correlations with the mAP_{50} metric at each point t . We compare these with the analogous correlations with the respective AUC at each point. Fig. 5 shows intensity diagrams representing the rank correlations both, in terms of image-wise and instance-wise

evaluation. The reference mark we chose is 90% of the maximum mAP_{50} obtained (*cf.* Tab. 2). The t -axes are normalized to the maximum number of images, resp. bounding boxes queried and the color indicates the Spearman correlation of the rankings. Red represents negative correlation (*i.e.* partial to full inversion of the observed ranking) while green means positive correlation (*i.e.* a higher degree of similarity of the rankings). In Fig. 5 both, mAP_{50} and AUC show overall high correlation with the method ranking, especially towards the end of the curves. We see that the correlations for AUC fluctuates far less. Moreover, the average correlation across entire AL curves tends to be larger for the AUC metric than mAP_{50} . Note that the final ranking of either method does not need to be perfectly correlated with the 90% max performance ranking for two reasons. Firstly, the latter does not take into consideration early performance gains and secondly, the 90% max performance ranking is a horizontal section through the curves while mAP_{50} and AUC are vertical sections. For a more quantitative evaluation, we show minimal and average correlation over all curves in Fig. 5. We observe overall high averages (upwards of 0.72) throughout the curves. The minimum AUC correlation tends to be higher than the minimum mAP_{50} correlation. We conclude that AUC tends to be highly correlated with the 90% max performance ranking and is more stable w.r.t. t than mAP_{50} .

Next, we study how comparable AL experiments are between the sandbox setting and full-complexity problems (VOC and BDD). To this end, we consider the cross-dataset correlations of the AUC score when fixing the detection architecture. Fig. 6 shows correlation matrices for image- and instance-wise evaluation. When comparing to the VOC-BDD correlations, the MNIST-Det and EMNIST-Det method rankings tend to be similarly correlated with either

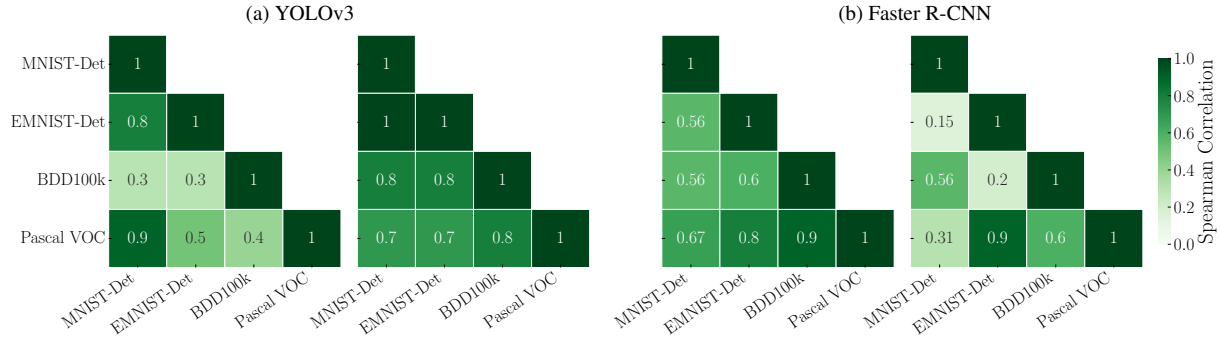


Figure 6: Ranking correlations between AUC values for different detectors, left: image-wise; right: instance-wise evaluation.

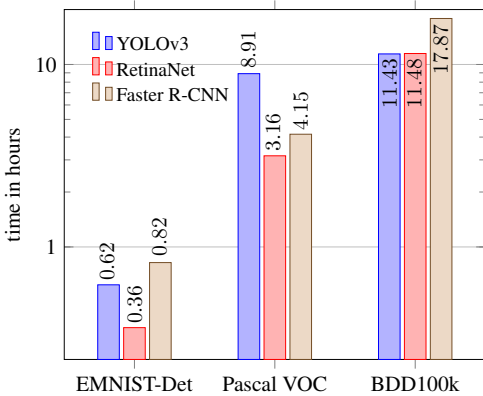


Figure 7: Utilized time for one AL step (training until convergence + evaluating the query) for investigated settings in hours.

one. Consider, for instance, the image-wise correlations on VOC. For the YOLOv3 detector, both MNIST-Det and EMNIST-Det have higher correlation with VOC than BDD does. Meanwhile, the BDD-MNIST-Det (resp. EMNIST-Det) correlation is a bit lower than VOC-BDD but similar. For Faster R-CNN, the correlation VOC-BDD is large with 0.9, however, both EMNIST-Det-VOC and EMNIST-Det-BDD have correlations of 0.6 and 0.8 which are reasonably high. For all correlations of VOC with BDD, replacing either one of the datasets with MNIST-Det or EMNIST-Det results in similar correlation. From this, we conclude that comparing methods in the simplified setting yields a similar amount of information about the relative performances of AL as the full-complexity setting.

4.3. Compute Time

AL for advanced image perception tasks such as OD tends to be highly time intensive, compute-heavy and energy consuming. This is due to the fact that at each AL step the model should be guaranteed to fit to convergence and there are multiple steps of (ideally) several random seeds to be

executed. Fig. 7 shows the time per AL step used in our setting when run on a Nvidia Tesla V100-SXM2-16GB GPU with a batch size of four. Note that the time-axis is scaled logarithmically, so the experiments on EMNIST-Det are always faster by at least half an order of magnitude. The training of YOLOv3 on VOC does not start from COCO-pretrained weights (like YOLOv3+BDD) since the two datasets VOC and COCO are highly similar and VOC consists of sub-classes of the COCO dataset. In this case, we opt for ImageNet-pretrained [26] backbone weights just like for the other detectors. We overall save time up to a factor of around 14 for VOC and around 32 for the BDD dataset. Translated to AL investigations, this means that the effects of new query strategies can be evaluated within half a day on a single Nvidia Tesla V100-SXM2-16GB.

5. Conclusion

In this work, we investigated the possibility of simplifying the active learning setting in deep object detection in order to accelerate development and evaluation time. We found that active learning curves do not trivially generalize from one (dataset, detector, evaluation metric)-constellation to another and that significant qualitative differences can be observed. Even though this prohibits the prediction of final method rankings we observe that the rank correlations are primarily positive and stay high throughout the active learning experiment. In our evaluation, we also included a more direct measurement of annotation effort in counting the number of queried instances in addition to the number of queried images. Meanwhile, we can save more than an order of magnitude in total compute time due to the down-scaling of the detection architecture and simplifying the dataset complexity. Our environment allows for consistent benchmarking of active learning methods in a unified object detection framework, thereby improving transparency. We hope that the present sandbox environment and findings along with the implemented framework will lead to further and accelerated progress in the field of active learning for object detection.

Acknowledgement. The research leading to these results is funded by the German Federal Ministry for Economic Affairs and Climate Action” within the projects “KI-Absicherung - Safe AI for Automated Driving”, grant no. 19A19005R and “KI Delta Learning - Scalable AI for Automated Driving”, grant no. 19A19013Q. We thank the consortia for the successful cooperation. We gratefully acknowledge financial support by the state Ministry of Economy, Innovation and Energy of Northrhine Westphalia (MWIDE) and the European Fund for Regional Development via the FIS.NRW project BIT-KI, grant no. EFRE-0400216. The authors gratefully acknowledge the **Gauss Centre for Supercomputing e.V.** for funding this project by providing computing time through the John von Neumann Institute for Computing on the GCS Supercomputer JUWELS at Jülich Supercomputing Centre.



References

- [1] Mohamed-Rafik Bouguelia, Yolande Belaïd, and Abdel Belaïd. Identifying and mitigating labelling errors in active learning. In *International Conference on Pattern Recognition Applications and Methods*, pages 35–51. Springer, 2015. [1](#)
- [2] Mohamed-Rafik Bouguelia, Slawomir Nowaczyk, KC Santosh, and Antanas Verikas. Agreeing to disagree: Active learning with noisy labels without crowdsourcing. *International Journal of Machine Learning and Cybernetics*, 9(8):1307–1319, 2018. [1](#)
- [3] Clemens-Alexander Brust, Christoph Käding, and Joachim Denzler. Active learning for deep object detection. *arXiv preprint arXiv:1809.09875*, 2018. [1](#), [2](#), [3](#), [13](#)
- [4] Samuel Budd, Emma C Robinson, and Bernhard Kainz. A survey on active learning and human-in-the-loop deep learning for medical image analysis. *Medical Image Analysis*, 71:102062, 2021. [1](#)
- [5] Kai Chen, Jiaqi Wang, Jiangmiao Pang, Yuhang Cao, Yu Xiong, Xiaoxiao Li, Shuyang Sun, Wansen Feng, Ziwei Liu, Jiarui Xu, Zheng Zhang, Dazhi Cheng, Chenchen Zhu, Tianheng Cheng, Qijie Zhao, Buyu Li, Xin Lu, Rui Zhu, Yue Wu, Jifeng Dai, Jingdong Wang, Jianping Shi, Wanli Ouyang, Chen Change Loy, and Dahua Lin. MMDetection: Open mmlab detection toolbox and benchmark. *arXiv preprint arXiv:1906.07155*, 2019. [5](#)
- [6] Jiwoong Choi, Ismail Elezi, Hyuk-Jae Lee, Clement Farabet, and Jose M Alvarez. Active learning for deep object detection via probabilistic modeling. In *Proceedings of the IEEE/CVF International Conference on Computer Vision*, pages 10264–10273, 2021. [1](#), [2](#), [3](#)
- [7] Gregory Cohen, Saeed Afshar, Jonathan Tapson, and Andre Van Schaik. Emnist: Extending mnist to hand-written letters. In *2017 international joint conference on neural networks (IJCNN)*, pages 2921–2926. IEEE, 2017. [2](#)
- [8] Ido Dagan and Sean P Engelson. Committee-based sampling for training probabilistic classifiers. In *Machine Learning Proceedings 1995*, pages 150–157. Elsevier, 1995. [2](#)
- [9] Sai Vikas Desai, Akshay Chandra Lagandula, Wei Guo, Seishi Ninomiya, and Vineeth N Balasubramanian. An adaptive supervision framework for active learning in object detection. In Kirill Sidorov and Yulia Hicks, editors, *Proceedings of the British Machine Vision Conference (BMVC)*, pages 177.1–177.13. BMVA Press, September 2019. [1](#), [3](#)
- [10] Ismail Elezi, Zhiding Yu, Anima Anandkumar, Laura Leal-Taixé, and Jose M. Alvarez. Not all labels are equal: Rationalizing the labeling costs for training object detection. In *Proceedings of the IEEE/CVF Conference on Computer Vision and Pattern Recognition (CVPR)*, pages 14492–14501, June 2022. [1](#), [3](#)
- [11] M. Everingham, L. Van Gool, C. K. I. Williams, J. Winn, and A. Zisserman. The pascal visual object classes (voc) challenge. *International Journal of Computer Vision*, 88(2):303–338, June 2010. [2](#)
- [12] Yarín Gal and Zoubin Ghahramani. Dropout as a bayesian approximation: Representing model uncertainty in deep learning. In *international conference on machine learning*, pages 1050–1059. PMLR, 2016. [2](#)
- [13] Yarín Gal, Riashat Islam, and Zoubin Ghahramani. Deep bayesian active learning with image data. In *International Conference on Machine Learning*, pages 1183–1192. PMLR, 2017. [2](#)
- [14] Elmar Haussmann, Michele Fenzi, Kashyap Chitta, Jan Ivaneky, Hanson Xu, Donna Roy, Akshita Mittel, Nicolas Koumchatzky, Clement Farabet, and Jose M Alvarez. Scalable active learning for object detection. In *2020 IEEE intelligent vehicles symposium (iv)*, pages 1430–1435. IEEE, 2020. [1](#), [2](#), [3](#)
- [15] Yann LeCun, Léon Bottou, Yoshua Bengio, and Patrick Haffner. Gradient-based learning applied to document recognition. *Proceedings of the IEEE*, 86(11):2278–2324, 1998. [2](#)
- [16] David D Lewis and Jason Catlett. Heterogeneous uncertainty sampling for supervised learning. In *Machine learning proceedings 1994*, pages 148–156. Elsevier, 1994. [2](#)

- [17] Mingkun Li and Ishwar K Sethi. Confidence-based active learning. *IEEE transactions on pattern analysis and machine intelligence*, 28(8):1251–1261, 2006. [1](#)
- [18] Tsung-Yi Lin, Priya Goyal, Ross Girshick, Kaiming He, and Piotr Dollár. Focal loss for dense object detection. In *Proceedings of the IEEE international conference on computer vision*, pages 2980–2988, 2017. [4](#)
- [19] Tsung-Yi Lin, Michael Maire, Serge Belongie, James Hays, Pietro Perona, Deva Ramanan, Piotr Dollár, and C Lawrence Zitnick. Microsoft coco: Common objects in context. In *European conference on computer vision*, pages 740–755. Springer, 2014. [2](#)
- [20] Yuval Netzer, Tao Wang, Adam Coates, Alessandro Bissacco, Bo Wu, and Andrew Y Ng. Reading digits in natural images with unsupervised feature learning. 2011. [3](#)
- [21] Hieu T Nguyen and Arnold Smeulders. Active learning using pre-clustering. In *Proceedings of the twenty-first international conference on Machine learning*, page 79, 2004. [2](#)
- [22] Dim P Papadopoulos, Jasper RR Uijlings, Frank Keller, and Vittorio Ferrari. Training object class detectors with click supervision. In *Proceedings of the IEEE Conference on Computer Vision and Pattern Recognition*, pages 6374–6383, 2017. [1](#), [3](#)
- [23] Joseph Redmon and Ali Farhadi. Yolov3: An incremental improvement. *arXiv preprint arXiv:1804.02767*, 2018. [4](#), [12](#)
- [24] Shaoqing Ren, Kaiming He, Ross Girshick, and Jian Sun. Faster r-cnn: Towards real-time object detection with region proposal networks. *Advances in neural information processing systems*, 28, 2015. [4](#)
- [25] Soumya Roy, Asim Unmesh, and Vinay P Namboodiri. Deep active learning for object detection. In *BMVC*, page 91, 2018. [1](#), [2](#), [3](#)
- [26] Olga Russakovsky, Jia Deng, Hao Su, Jonathan Krause, Sanjeev Satheesh, Sean Ma, Zhiheng Huang, Andrej Karpathy, Aditya Khosla, Michael Bernstein, Alexander C. Berg, and Li Fei-Fei. ImageNet Large Scale Visual Recognition Challenge. *International Journal of Computer Vision (IJCV)*, 115(3):211–252, 2015. [8](#)
- [27] Tobias Scheffer, Christian Decomain, and Stefan Wrobel. Active hidden markov models for information extraction. In *International Symposium on Intelligent Data Analysis*, pages 309–318. Springer, 2001. [2](#)
- [28] Sebastian Schmidt, Qing Rao, Julian Tatsch, and Alois Knoll. Advanced active learning strategies for object detection. In *2020 IEEE Intelligent Vehicles Symposium (IV)*, pages 871–876. IEEE, 2020. [1](#), [2](#)
- [29] Ozan Sener and Silvio Savarese. Active learning for convolutional neural networks: A core-set approach. In *International Conference on Learning Representations*, 2018. [2](#)
- [30] B. Settles. Active learning literature survey. Computer Sciences Technical Report 1648, University of Wisconsin–Madison, 2009. [1](#), [2](#), [3](#)
- [31] H Sebastian Seung, Manfred Opper, and Haim Sompolinsky. Query by committee. In *Proceedings of the fifth annual workshop on Computational learning theory*, pages 287–294, 1992. [2](#)
- [32] Adithya Subramanian and Anbumani Subramanian. One-click annotation with guided hierarchical object detection. *arXiv preprint arXiv:1810.00609*, 2018. [1](#), [3](#)
- [33] Akim Tsvigun, Artem Shelmanov, Gleb Kuzmin, Leonid Sanochkin, Daniil Larionov, Gleb Gusev, Manvel Avetisian, and Leonid Zhukov. Towards computationally feasible deep active learning. *arXiv preprint arXiv:2205.03598*, 2022. [1](#)
- [34] Zuobing Xu, Ram Akella, and Yi Zhang. Incorporating diversity and density in active learning for relevance feedback. In *European Conference on Information Retrieval*, pages 246–257. Springer, 2007. [2](#)
- [35] Donggeun Yoo and In So Kweon. Learning loss for active learning. In *Proceedings of the IEEE/CVF conference on computer vision and pattern recognition*, pages 93–102, 2019. [1](#), [2](#)
- [36] Taraneh Younesian, Dick Epema, and Lydia Y Chen. Active learning for noisy data streams using weak and strong labelers. *arXiv preprint arXiv:2010.14149*, 2020. [1](#)
- [37] Taraneh Younesian, Zilong Zhao, Amirmasoud Ghiasi, Robert Birke, and Lydia Y Chen. Qactor: Active learning on noisy labels. In *Asian Conference on Machine Learning*, pages 548–563. PMLR, 2021. [1](#)
- [38] Fisher Yu, Haofeng Chen, Xin Wang, Wenqi Xian, Yingying Chen, Fangchen Liu, Vashisht Madhavan, and Trevor Darrell. Bdd100k: A diverse driving dataset for heterogeneous multitask learning. In *Proceedings of the IEEE/CVF conference on computer vision and pattern recognition*, pages 2636–2645, 2020. [2](#)
- [39] Tianning Yuan, Fang Wan, Mengying Fu, Jianzhuang Liu, Songcen Xu, Xiangyang Ji, and Qixiang Ye. Multiple instance active learning for object detection. In *Proceedings of the IEEE/CVF Conference on Computer Vision and Pattern Recognition*, pages 5330–5339, 2021. [1](#), [2](#)
- [40] Xueying Zhan, Qingzhong Wang, Kuan-hao Huang, Haoyi Xiong, Dejing Dou, and Antoni B Chan. A

comparative survey of deep active learning. *arXiv preprint arXiv:2203.13450*, 2022. [1](#)

Supplementary Material to:
**Towards Rapid Prototyping and
Comparability in Active Learning for
Deep Object Detection**

A. Implementation Details

A.1. OD Architectures

In our experiments we used a YOLOv3 detector with the standard Darknet53 backbone on VOC and BDD. In our down-scaled version we replace the backbone with an analogous architecture working on the same resolutions, such that all strides remain the same and the detection mechanism works identically. Tab. 5 shows the configuration comparison between the standard Darknet53 architecture and our adapted version (here, called Darknet20) which significantly reduces depth and the number of feature channels extracted. All other model and data augmentation configurations remain unchanged.

For Faster R-CNN we use a ResNet101 backbone on VOC and BDD while for RetinaNet, we use a ResNet50. Here, we use a Feature Pyramid Network (FPN) with [256, 512, 1024, 2048] channels. Both are down-scaled to ResNet18 backbones with [64, 128, 256, 512]-channel FPN to accelerate training and inference.

For all architectures, we insert dropout layers between the two last layers (convolutional layers at all stages for YOLOv3/RetinaNet and fully connected for Faster R-CNN). For all experiments involving sampling, *i.e.*, MC Dropout and Mutual Information experiments, we use dropout rates of 0.5 and perform 10 forward passes.

A.2. Dataset Variability

When comparing to existing OD datasets, our sandbox datasets MNIST-Det and EMNIST-Det resemble in variability the common benchmarks like Pascal VOC, MS COCO, KITTI or BDD100k. This can be seen when looking at the

Table 4: Standard deviations of center coordinates, width and height (all relative to image size) of bounding boxes, as well, as number of categories in the training split for several object detection datasets.

Dataset	c_x	c_y	w	h	# categories
SVHN	0.099	0.059	0.048	0.161	10
Pascal VOC	0.217	0.163	0.284	0.277	20
MS COCO	0.254	0.209	0.220	0.234	80
KITTI	0.229	0.080	0.067	0.157	8
BDD100k	0.224	0.133	0.059	0.086	10
MNIST-Det	0.233	0.233	0.054	0.054	10
EMNIST-Det	0.233	0.233	0.066	0.065	26

Table 5: Configuration of Darknet20 compared with Darknet53 in analogy to [23, Tab. 1]. At equal resolution input, the feature maps also remain at the same resolution at each stage.

Type	Size	Darknet53		Darknet20	
		Blocks	Filters	Blocks	Filters
Conv	3×3		32		32
Conv	$3 \times 3/2$		64		32
Conv	1×1		32		32
Conv	3×3	1×	64	1×	64
Residual					
Conv	$3 \times 3/2$		128		64
Conv	1×1		64		32
Conv	3×3	2×	128	1×	64
Residual					
Conv	$3 \times 3/2$		256		128
Conv	1×1		128		64
Conv	3×3	8×	256	1×	128
Residual					
Conv	$3 \times 3/2$		512		256
Conv	1×1		256		128
Conv	3×3	8×	512	2×	256
Residual					
Conv	$3 \times 3/2$		1024		512
Conv	1×1		512		256
Conv	3×3	4×	1024	2×	512
Residual					

variations in bounding box localization across each dataset. When normalizing to the total image resolution, we can compare the standard deviations in the annotation center coordinates c_x , c_y as well as the bounding box extent w and h , which we have collected in Tab. 4. The SVHN dataset consisting of photographs of house numbers shows little variability, especially in the center localization of the object (which are mostly centered on the image). Figure 12 shows samples from the MNIST-Det and EMNIST-Det datasets.

A.3. AL Parameters

Tab. 6 gives an overview of chosen hyperparameters for the AL cycle for all datasets and architectures. Thereby, $|\mathcal{U}_{init}|$ stands for the number of initially annotated images, $|\mathcal{Q}|$ for the size of the selected query, ϵ_s for the score threshold for query inference (thereby, determining instance-wise uncertainty) and T for number of AL steps. The hyperparameters for training are the batch size, which is always 4, the number of training iterations, and the image resolution. It follows from Tab. 6 (particularly, $|\mathcal{U}_{init}|$, $|\mathcal{Q}|$ and T) that all architectures considered in our experiments

Table 6: Overview of important AL hyperparameters for querying data and model training for all datasets and architectures.

		$ \mathcal{U}_{init} $	$ \mathcal{Q} $	Query			Training		
				ϵ_s	image resolution	T	batch size	training iters	image resolution
YOLOv3	MNIST-Det	100	50	0.5	300×300	8	4	35,000	300×300
	EMNIST-Det	100	100	0.5	320×320	8	4	50,000	320×320
	Pascal VOC	200	150	0.5	608×608	15	4	18,750*	[(320, 320), (608, 608)]
	BDD100k	1,100	700	0.5	608×608	8	4	160,000	[(320, 320), (608, 608)]
FRCNN	MNIST-Det	100	50	0.7	300×300	8	4	30,000	300×300
	EMNIST-Det	100	100	0.7	320×320	8	4	30,000	320×320
	Pascal VOC	100	100	0.7	1000×600	15	4	18,750	1000×600
	BDD100k	1,250	750	0.7	1000×600	8	4	170,000	1000×600
RetinaNet	MNIST-Det	100	50	0.5	300×300	8	4	25,000	300×300
	EMNIST-Det	225	125	0.5	300×300	8	4	35,000	300×300
	Pascal VOC	550	350	0.5	1000×600	8	4	60,000	1000×600
	BDD100k	1,000	500	0.5	1000×600	8	4	175,000	1000×600

need the fewest images for our sandbox datasets MNIST-Det and EMNIST-Det to reach the 90% max performance mark. Therefore, for the sandbox datasets we chose $|\mathcal{U}_{init}|$ and $|\mathcal{Q}|$ smaller than for VOC and BDD. Moreover, the sandbox datasets have lower image resolutions, which leads to faster training and inference times, even if occasionally the training iterations are lower for VOC, *e.g.*, for Faster R-CNN and YOLOv3. Apart from the latter case, the most iterations to obtain convergence in the training processes are needed for BDD with up to 175,000. The score threshold of 0.5 for YOLOv3 and RetinaNet, and 0.7 for Faster R-CNN was determined by ablation studies for EMNIST-Det and then adopted for the other datasets. For all query methods, we incorporate a class-weighting (the same as in [3]) for computing instance-wise uncertainty scores.

B. Ablations

B.1. Image-aggregation Methods

Figure 8 shows test mAP_{50} for different image aggregations, namely sum, average and maximum, for the RetinaNet on EMNIST-Det. The left panels show mAP_{50} scores as a function of the number of queried images while the right panels show mAP_{50} scores as a function of the number of queried instances. For all four uncertainty baselines, the sum dominates the maximum and the maximum dominates the average in the image-wise evaluation. Nevertheless, the average remains consistently better than Random, with the exception of Mutual Information, where both curves are almost on par. A clearly different course is obtained when considering the instance-wise evaluation. For the same number of images queried, the sum prefers images with many boxes, whereas the average queries images with even fewer boxes than the Random baseline. In terms of performance, the average outperforms the sum and maxi-

um, which are tied, and the Random baseline for Entropy and Probability Margin. For Mutual Information, the average and sum are best, whereas for MC Dropout all curves are hardly distinguishable from each other. Comparable behaviors could also be observed on the other architectures and datasets.

Investigations of the kind presented here under normal conditions (using a full-scale standard object detector and a benchmark dataset) would require weeks of compute time and yield valuable information on sensitive parameters for querying. Using our sandbox environment makes extensive ablation studies of hyperparameters possible within a few days.

C. Additional Numerical Results

In this section, we compile additional experimental results supplementing Tab. 3 from the main manuscript with additional metrics and results from the RetinaNet detector which were struck from the main part due to spacial constraints.

C.1. Benchmark Results

Table 7 shows the mAP_{50} achieved after the final query for each method and detector-dataset constellation in the style of Tab. 3. For each AL curve, the final performance (most queried images allowed according to Tab. 6) is independent of an image- or instance-wise point of view. Overall, the Entropy baseline is consistently among the best two methods, however, the overall rankings show a medium degree of variance across datasets and across detectors especially when regarding instance-wise evaluation in Tab. 3.

*If the training process for YOLOv3 on VOC is trained with pre-trained ImageNet weights instead of COCO weights, the number of training iterations increases from 18,750 to 200,000.

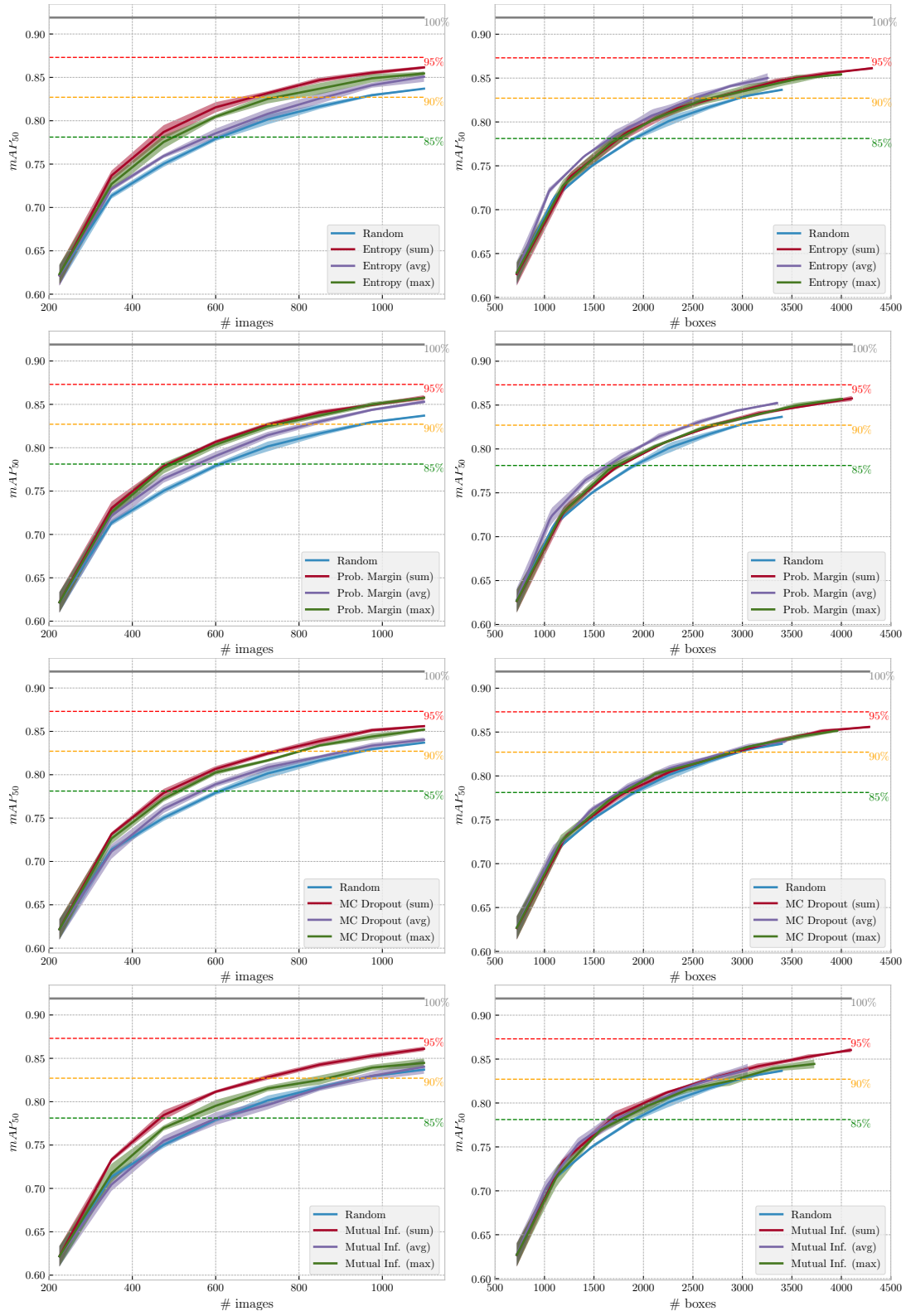


Figure 8: Ablation study on the aggregation method for RetinaNet on the EMNIST-Det dataset.

Table 7: Mean average precision results per query method for maximal amount of images selected; higher values are better. Bold numbers indicate the highest performance per experiment and underlined numbers are the second highest.

		MNIST-Det	EMNIST-Det	Pascal VOC	BDD100k
YOLOv3	Random	89.28	88.95	72.10	38.22
	Entropy	91.53	91.75	73.08	<u>39.28</u>
	Prob. Margin	91.03	<u>91.42</u>	72.65	39.35
	MC Dropout	<u>91.08</u>	<u>91.42</u>	<u>72.78</u>	38.80
	Mutual Inf.	91.05	<u>91.42</u>	72.22	38.30
Faster R-CNN	Random	83.20	83.92	74.67	47.02
	Entropy	<u>85.27</u>	87.15	75.10	<u>48.30</u>
	Prob. Margin	85.00	86.62	75.40	48.35
	MC Dropout	85.28	86.05	74.25	47.27
	Mutual Inf.	<u>85.27</u>	<u>87.07</u>	74.35	47.27
RetinaNet	Random	82.95	83.70	69.58	43.20
	Entropy	85.35	86.15	71.80	43.97
	Prob. Margin	84.38	85.78	<u>71.55</u>	<u>43.75</u>
	MC Dropout	85.02	85.60	68.17	43.50
	Mutual Inf.	<u>85.33</u>	<u>86.10</u>	68.12	43.48

Comparing vertical sections through AL curves shows overall roughly similar behavior as the results in Tab. 3 (horizontal sections), however, we observe differences in the method rankings in terms of amount of data queried vs. final detection performance (e.g., Faster R-CNN on the MNIST-Det dataset).

In Tab. 8 we collect the values of the AUC metric. Note, that the AUC metric scales with the t -axis, i.e., results between different datasets can only be compared qualitatively. The same is true for comparisons between image- and instance-wise evaluations. When comparing with Tab. 3 from Section 4.1, we see a high degree of ranking similarity with the amount of data required to cross the 90%-mark in both, image- and instance-wise evaluation. We conclude with previous findings on the rank correlations, that even in a rather late evaluation (when some fixed reference mark in performance has already been crossed), the AUC shows more similarity with the 90% ranking than raw detection performance (Tab. 7). For instance, compare the Faster R-CNN row from Tab. 3 with the corresponding row in Tab. 8.

We include results for the RetinaNet detection analogous to Tab. 3 in Tab. 9. Again, we notice striking ranking differences between image- and instance-wise evaluation. Particularly, instance-wise evaluation has rather irregular method rankings between datasets for the RetinaNet detector which were, however, also reflected in our AUC evaluation discussed before in Tab. 8. These results yield further evidence that the consideration of only a single evaluation metric for active learning performance is insufficient.

C.2. Generalization on RetinaNet

Ranking correlations for mAP_{50} and AUC for RetinaNet, see Fig. 9, tend to show the same behavior as for the YOLOv3 and Faster R-CNN. The AUC fluctuates less than

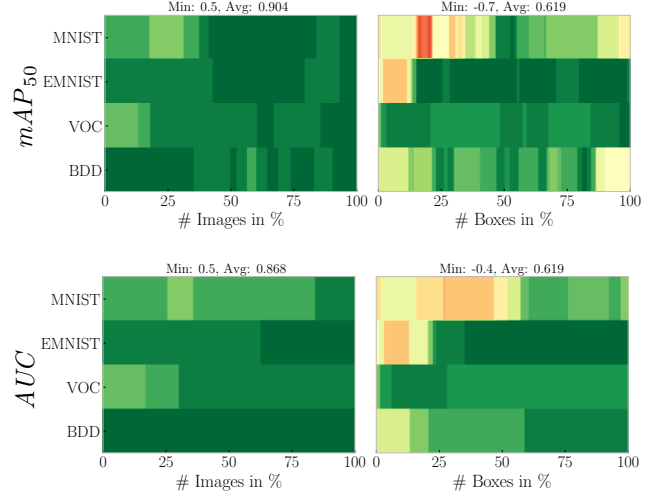


Figure 9: Curves of rank correlations between the cumulative AUC and the final rankings at the 90% max performance mark for the RetinaNet detector.

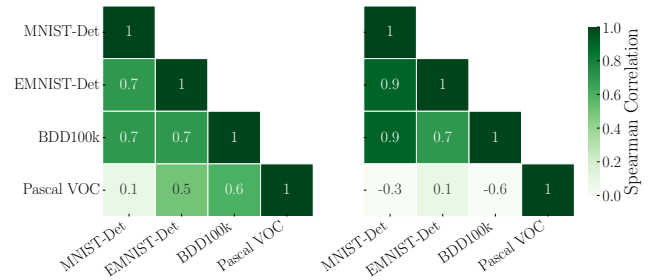


Figure 10: Ranking correlations between AUC values for the RetinaNet detector, left: image-wise; right: instance-wise evaluation.

the mAP_{50} and both metrics show overall high correlation with the 90% max performance ranking. For the image-wise evaluation, both metrics have correlations greater or equal than 0.5. In the instance-wise evaluation, on the other hand, the correlations increase only gradually. Even though the average correlations are identical for the mAP_{50} and the AUC , the latter is clearly more stable w.r.t. the 90% max performance ranking and has a higher minimum correlation.

Figure 10 shows correlation matrices for the RetinaNet. The image-wise comparison shows the highest correlation of 0.7 when comparing MNIST-Det, EMNIST-Det and BDD respectively. VOC has the highest correlation with BDD of 0.6, but the correlation with EMNIST-Det is similar with 0.5. No conclusions can be drawn between the rankings of MNIST-Det and VOC due to the low correlation of 0.1. In the instance-wise comparison, MNIST-Det has very high correlations of 0.9 with EMNIST-Det and BDD, and the comparability of the rankings of EMNIST-Det and BDD is also given by a correlation of 0.7. How-

Table 8: Area under AL curve results per query method for maximal amount of data (images/bounding boxes) selected; higher values are better. Bold numbers indicate the highest AUC per experiment and underlined numbers are the second highest.

		# queried images				# queried bounding boxes			
		MNIST-Det	EMNIST-Det	Pascal VOC	BDD100k	MNIST-Det	EMNIST-Det	Pascal VOC	BDD100k
YOLOv3	Random	290.9	543.3	1645.1	1691.9	1503.8	2438.7	4274.3	37327.3
	Entropy	299.6	<u>577.4</u>	1685.2	<u>1728.8</u>	1519.0	2491.4	4324.6	<u>37816.6</u>
	Prob. Margin	298.1	571.9	1664.5	1733.6	<u>1516.2</u>	<u>2485.3</u>	<u>4303.4</u>	37931.1
	MC Dropout	298.3	571.8	<u>1684.9</u>	1727.9	1503.8	2465.5	4284.6	37550.7
	Mutual Inf.	<u>299.1</u>	578.0	1666.8	1716.1	1509.4	2482.6	4233.2	37514.5
Faster R-CNN	Random	273.0	542.6	1207.9	2220.1	1448.6	2643.7	3121.5	47767.9
	Entropy	281.3	567.1	1237.6	<u>2266.7</u>	1465.2	2703.6	3168.8	<u>48167.8</u>
	Prob. Margin	279.7	561.3	<u>1236.4</u>	2274.7	1465.2	<u>2692.5</u>	<u>3168.3</u>	48449.2
	MC Dropout	<u>280.5</u>	557.0	1227.0	2247.3	1451.4	2619.7	3052.8	47718.9
	Mutual Inf.	280.2	<u>566.6</u>	1230.5	2247.8	<u>1457.5</u>	2697.4	3123.8	47714.8
RetinaNet	Random	270.4	677.5	1743.6	1380.5	1438.2	2896.9	4614.9	33141.5
	Entropy	279.1	701.9	1819.7	1421.6	<u>1446.2</u>	<u>2932.4</u>	<u>4714.6</u>	33431.4
	Prob. Margin	276.8	696.5	<u>1802.8</u>	<u>1414.7</u>	1445.6	2928.4	4722.5	33339.5
	MC Dropout	<u>279.0</u>	696.3	1730.6	1406.2	1445.6	2915.8	4535.9	<u>33452.9</u>
	Mutual Inf.	278.5	<u>699.3</u>	1734.7	1400.8	1449.1	2940.7	4543.9	33495.2

Table 9: Amount of queried images and bounding boxes necessary to cross the 90% performance mark during AL for the RetinaNet detector. Lower values are better. Bold numbers indicate the lowest amount of data per experiment and underlined numbers are the second lowest.

		# queried images				# queried bounding boxes			
		MNIST-Det	EMNIST-Det	Pascal VOC	BDD100k	MNIST-Det	EMNIST-Det	Pascal VOC	BDD100k
RetinaNet	Random	390.3	950.4	2555.4	3616.2	1283.8	2957.7	6220.0	69842.0
	Entropy (sum)	288.6	687.7	1961.2	2866.5	1292.0	<u>2708.6</u>	5421.6	64939.7
	Prob. Margin (sum)	310.8	733.9	<u>2087.3</u>	<u>2901.5</u>	<u>1277.5</u>	2721.5	<u>5445.6</u>	64794.9
	MC Dropout (sum)	293.3	749.6	2745.3	3027.7	1317.4	2926.4	7047.9	<u>62395.5</u>
	Mutual Inf. (sum)	<u>289.6</u>	<u>719.0</u>	2881.9	3124.9	1248.0	2677.4	7389.0	61712.9

ever, it is again noticeable that VOC is hardly comparable with any other dataset. This could be attributed to some of the dataset characteristics. On one hand, we observed many missing labels when looking at the VOC data (*cf.* Fig. 11). On the other hand, the instance sizes of BDD and EMNIST-Det/MNIST-Det seem to be rather comparable as opposed to the instance sizes in VOC.



Figure 11: Annotation examples from the Pascal VOC test dataset.

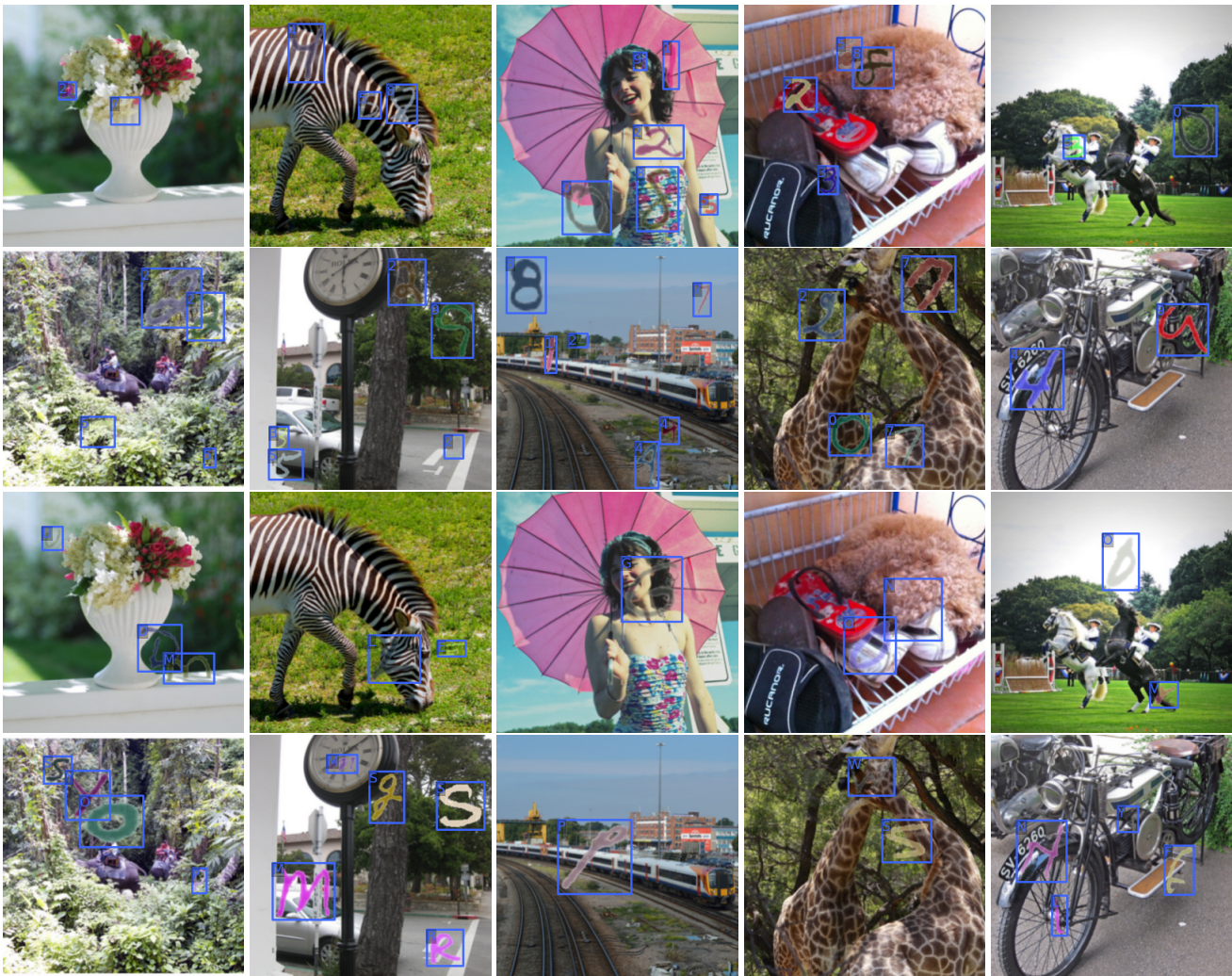


Figure 12: Dataset samples from MNIST-Det (top three rows) and EMNIST-Det (bottom three rows) including annotations.